

# Influence of rare earth ( $\text{Nd}^{+3}$ ) doping on structural and magnetic properties of nanocrystalline manganese-zinc ferrite

Pranav P. Naik <sup>a,\*</sup>, R.B. Tangsali <sup>a</sup>, S.S. Meena <sup>b</sup>, S.M. Yusuf <sup>b</sup>

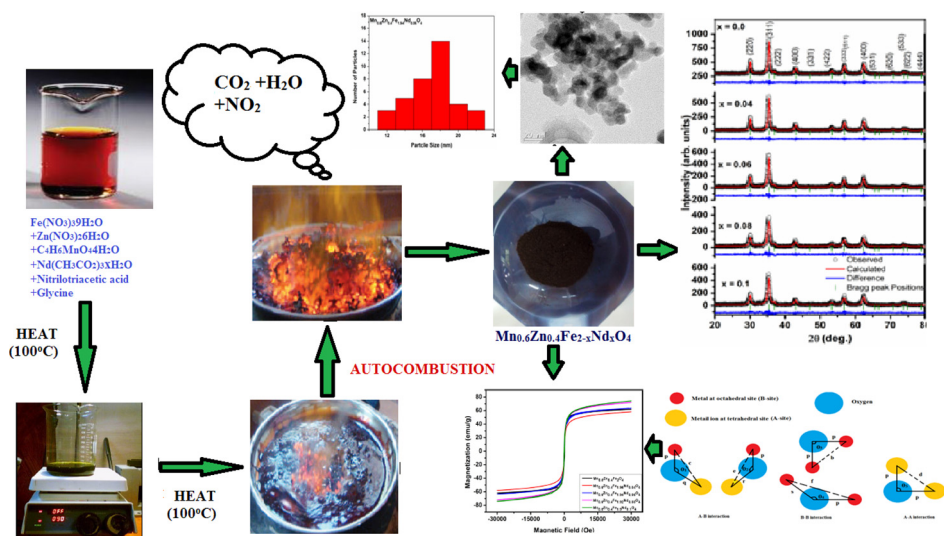
<sup>a</sup> Department of Physics, Goa University, Taleigao Plateau, Goa, 403206, India

<sup>b</sup> Solid State Physics Division, Bhabha Atomic Research Centre, Mumbai, 400085, India

## HIGHLIGHTS

- Synthesis of Nd doped Mn-Zn ferrite nanoparticles using combustion method.
- Successful doping of  $\text{Nd}^{+3}$  at octahedral site in ferrite structure.
- Existence of  $\text{Fe}^{+3}$  oxidation state at both A-Site and B-site.
- Enhanced saturation magnetization due to altered cation distribution by Nd doping.
- Reduction in A-site hyperfine field.

## GRAPHICAL ABSTRACT



## ARTICLE INFO

### Article history:

Received 15 July 2016

Received in revised form

4 November 2016

Accepted 9 January 2017

Available online 11 January 2017

### Keywords:

Nanoparticles  
Saturation magnetization  
Isomer shift  
Hyperfine field  
Cation distribution

## ABSTRACT

Ultrafine nanopowders of Mn<sub>0.6</sub>Zn<sub>0.4</sub>Fe<sub>2-x</sub>Nd<sub>x</sub>O<sub>4</sub> ( $x = 0, 0.04, 0.06, 0.08$ , and  $0.1$ ) were prepared using combustion method. The influence of Nd<sup>+3</sup> doping on structural parameters, morphological characteristics and magnetic properties were investigated. Formation of pure spinel phase was confirmed using X-ray powder diffraction (XRPD). Nd<sup>+3</sup> doping in Mn-Zn ferrite samples have shown remarkable influence on all the properties that were under investigation. An increase in lattice constant commensurate with increasing Nd<sup>+3</sup> concentrations was observed in the samples. The crystallite size calculated from XRPD data and grain size observed from Transmission Electron Microscope showed a proportionate decrement with increment in rare earth doping. An increase in mass density, X-ray density, particle strain and decrease in porosity were the other effects noticed on the samples as a result of Nd<sup>+3</sup> doping. The corresponding tetrahedral, octahedral bond lengths and bond angles estimated from XRPD data have also shown substantial influence of the Nd<sup>+3</sup> doping. Magnetic parameters namely saturation magnetization ( $M_s$ ) and net magnetic moment  $\eta_B$ , estimated using vibrating sample magnetometer (VSM) were found to depend on the Nd<sup>+3</sup> doping. Mössbauer spectroscopy was employed to study the magnetic

\* Corresponding author.

E-mail address: [drppn1987@gmail.com](mailto:drppn1987@gmail.com) (P.P. Naik).



environment of Mössbauer active ions and detection of superparamagnetic behavior in nanocrystalline rare earth ferrite material. The isomer shift values obtained from Mössbauer spectra indicate the presence of  $\text{Fe}^{+3}$  ions at tetrahedral site (A-site) and octahedral site (B-site), respectively.

© 2017 Elsevier B.V. All rights reserved.

## 1. Introduction

Ferrimagnetic spinel material, Manganese Zinc ferrite constitutes an important class of ceramic materials that has been under investigation since several decades [1,2]. Their structural, magnetic and electrical properties are interesting and typically depend on the nature of their cation distribution over tetrahedral site (A-site) and octahedral site (B-site) [3–7]. These materials have wide range of technological and scientific application in electronics, optoelectronics, refrigeration, magnetic recording media, magneto caloric applications, sensors etc. These are also used in temperature sensitive ferrofluids for applications in heat transfer enhancement, energy conversion devices and power devices especially for electromagnetic interference suppression (EMIS) [8–11]. The wide spectrum of application based unique properties of manganese zinc ferrite depend upon various features of the material such as grain size, type and concentrations of doping as well as cation distribution which are directly linked to the conditions at the time of material preparation. In the early period of investigations ferrite materials were prepared by a ceramic process involving high temperature solid state reactions between the constituent oxides/carbonates. Materials obtain by this method did suffer from several imperfections including structural anomalies. Obtaining pure monophasic material using this method has been an intricate exercise. Moreover the method never yielded high purity material with uniform particles size distribution. This method of sample preparation is not suitable for production of nanoparticle sample. However with the development of new methods of materials preparation such as co-precipitation method [12,13], the hydrothermal precipitation processing [14], the sol-gel synthesis [15], the micro-emulsion approach [16,17] combustion synthesis [18–20], and spray pyrolysis [21] one could prepare nanoparticle Mn-Zn ferrite material with more refined structure and properties suitable for high end applications and research. Application of high energy ion beams and high energy radiation in materials preparation has also played a significant role in alteration of structural properties and enrichment of some material properties of the samples. Reports on these materials show that, post synthesis alteration in structural, morphological, magnetic and electrical properties can also be introduced by exposing these materials to high energy radiation gamma radiation. The alterations introduced by this route are of permanent nature and are proportional to the radiation dose intensity and time of exposure [22–25]. Alternately it is possible to produce similar changes by augmenting the chemical composition of these materials by introduction of rare earth (RE) ions with larger ionic radii. Small rare earth substitution can replace Fe at octahedral site and bring about a drastic change in their structure and properties as well [26–28]. It is observed that even small substitutions of rare earths can replace Fe ions at B site that may lead to the enhancement the magnetic and electrical properties of ferrite resulting in a good magnetic material suitable for high frequency applications. Rare earth (RE) ions have unpaired 4f electrons, which are responsible for originating magnetic anisotropy due to their orbital shape. The magneto-crystalline anisotropy in ferrite is related to the 3d-4f couplings between the transition metal and rare earth ions; thus, doping rare earth ions

into spinel ferrite can improve their electrical and magnetic properties [29]. One of the major difficulties associated with such doping is limited solubility of rare earth ions in Mn-Zn ferrite host material. Thus it was worthwhile to investigate the properties of rare-earth doped Mn-Zn ferrite nanoparticles, as expected refinement in structure leading to enhancement of magnetic properties could be obtained by rare earth substitution, that could probably occur at B site. In the present article we report interesting findings that transpired out of the explorations carried out on  $\text{Nd}^{+3}$  doped nanoparticle  $\text{Mn}_{0.6}\text{Zn}_{0.4}\text{Fe}_{2-x}\text{Nd}_x\text{O}_4$  ( $x = 0, 0.04, 0.06, 0.08$ , and  $0.1$ ) Manganese Zinc Ferrite prepared by combustion synthesis.

## 2. Experimental

Ultrafine nanopowders of  $\text{Mn}_{0.6}\text{Zn}_{0.4}\text{Fe}_{2-x}\text{Nd}_x\text{O}_4$  ( $x = 0.00, 0.04, 0.06, 0.08$  and  $0.1$ ) were prepared using combustion synthesis method. Metal salts  $\text{Fe}(\text{NO}_3)_3 \cdot 9\text{H}_2\text{O}$ ,  $\text{Zn}(\text{NO}_3)_2 \cdot 6\text{H}_2\text{O}$ ,  $\text{C}_4\text{H}_6\text{MnO}_4 \cdot 4\text{H}_2\text{O}$  and  $\text{Nd}(\text{CH}_3\text{CO}_2)_3 \cdot x\text{H}_2\text{O}$  were taken in proportionate quantity along with Nitrilotriacetic acid as complexing agent which also facilitates the process of combustion and Glycine as fuel. All the metal salts were dissolved in distilled water at certain elevated temperature to obtain a clear solution. The solution was subjected to volume reduction by conventional heating till the auto-combustion was triggered. The temperature at this stage approaches a maximum value of approximately  $650^\circ\text{C}$ – $700^\circ\text{C}$ . The residual powders obtained from the combustion process were the actual samples that were subjected to various characterization techniques. The method employed is quick, simple, and cost effective and provides narrow dispersion in grain size distribution [30–32]. Investigations for phase confirmation were done using Rigaku X-ray diffractometer (Bragg Brentano geometry,  $\text{Cu}-\text{k}_\alpha$ ,  $\lambda = 1.5418 \text{\AA}$ ) over the  $2\theta$  range of  $20^\circ$  to  $80^\circ$  in steps of  $0.02^\circ$  and at scan rate of  $2^\circ/\text{min}$ . Rietveld refinement of XRPD data obtained on these samples was done using FullProf suit software. Fourier transform infrared spectra were recorded on Shimadzu FTIR 8900 assembly. Particle size estimation was done using Hitachi transmission electron microscope. Mössbauer spectra of these samples were recorded using conventional Mössbauer spectrometer in constant acceleration mode with Co-57 radioactive source embedded in rhodium matrix of 50 mCi. Magnetic properties were measured using Quantum Design Versa Lab 3T vibrating sample magnetometer (VSM).

## 3. Results and discussion

### 3.1. X-ray powder diffraction (XRD)

**Fig. 1(a)** shows the Rietveld analysis of XRPD patterns obtained for the  $\text{Mn}_{0.6}\text{Zn}_{0.4}\text{Fe}_{2-x}\text{Nd}_x\text{O}_4$  samples with  $x = 0.0, 0.04, 0.06, 0.08$ , and  $0.1$ .

The indexed Rietveld refined XRPD patterns clearly confirm formation of pure monophasic spinel structure samples [33–35]. The agreement values  $R_{wp}$ ,  $R_p$ ,  $R_{exp}$ ,  $R_{Bragg}$  and  $\chi^2$  along with oxygen parameter ‘u’ for as prepared samples are listed in **Table 1**. Crystallite size was calculated from full width at half-maximum of the (311) peak in the XRPD pattern using the Scherrer's formula

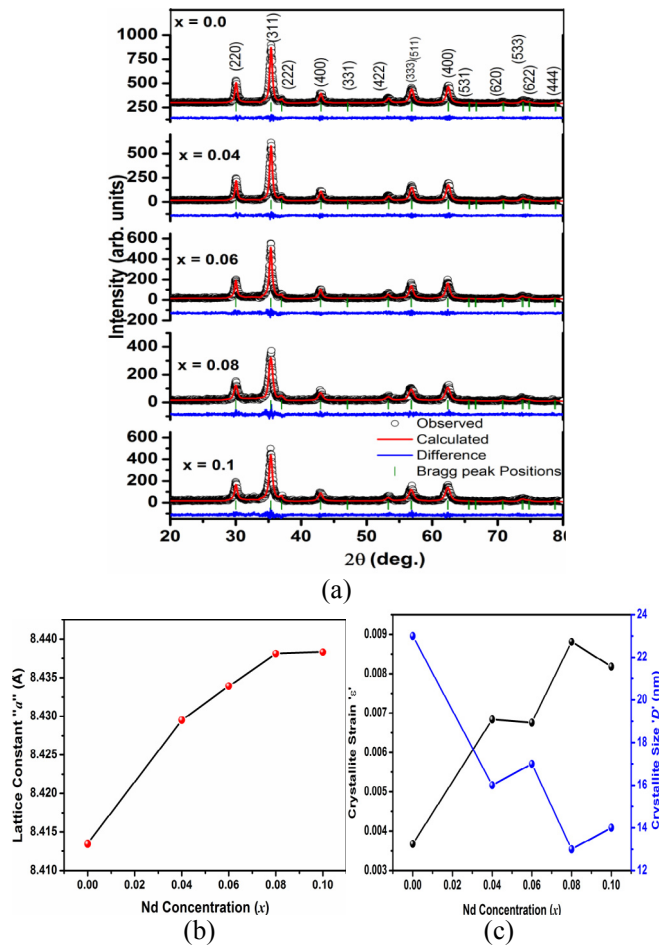


Fig. 1. (a) Rietveld analysis of X-ray powder diffraction pattern for  $Mn_{0.6}Zn_{0.4}Fe_{2-x}Nd_xO_4$  nanopowders, (b) Variation of lattice constant 'a' (c) Variation of crystallite size 'D' and crystallite strain 'e' with Nd concentration (x).

Table 1

Variation of agreement values oxygen parameter 'u',  $R_{wp}$ ,  $R_p$ ,  $R_{exp}$ ,  $R_{Bragg}$  and  $\chi^2$  obtained from Rietveld refinement of XRPD patterns of  $Mn_{0.6}Zn_{0.4}Fe_{2-x}Nd_xO_4$ .

Samples $Mn_{0.6}Zn_{0.4}Fe_{2-x}Nd_xO_4$	Oxygen parameter 'u'	$R_{wp}$	$R_p$	$R_{exp}$	$R_{Bragg}$	$\chi^2$
x = 0.0	0.3746(3)	21.3	16.3	14.3	4.56	1.29
x = 0.04	0.3742(5)	23.5	17.5	15.01	6.31	1.36
x = 0.06	0.3739(2)	22.7	18.7	15.37	6.49	1.48
x = 0.08	0.3737(5)	24.6	21.1	17.11	7.23	1.52
x = 0.1	0.3735(7)	29.3	22.4	17.87	7.48	1.57

(Equation (1)). Crystallite strain was calculated using Equation (2) [36,37].

$$D = 0.9\lambda/\beta(\cos\theta) \quad (1)$$

$$\epsilon = \beta/(4 \cos \theta) \quad (2)$$

The variation of lattice constant 'a' and unit cell volume as a function  $Nd^{+3}$  concentrations is shown in Fig. 1(b) and (c) respectively.

The lattice parameter 'a' is found to increase almost steeply with increasing  $Nd^{+3}$  concentrations up to  $x = 0.08$  after which it nearly remains stagnant at  $x = 0.1$ . This feature can be attributed to the larger ionic radii of  $Nd^{+3}$  ion ( $1.12 \text{ \AA}$ ) which replaces  $Fe^{3+}$  ( $0.64 \text{ \AA}$ ) at octahedral site resulting in overall expansion in lattice dimensions

and hence unit cell volume. The stagnant behavior of the lattice constant between  $x = 0.08$  and  $0.1$  may be due to optimum occupation of octahedral sites by  $Nd^{+3}$  at  $x = 0.08$  which develops maximum strain within the lattice at this concentration which exhibits a minor relaxation in strain on further increase  $Nd^{+3}$  doping. This behavior is evident from first curve shown in Fig. 1(c). Comparison of the two curves in Fig. 1(c) clearly shows the dependence of crystallite strain on the crystallite size that can be linked to the lattice constant curves given in Fig. 1 (b). Induced strain in the lattice due to inclusion of rare earth at octahedral site hinders the crystallite growth that results in synthesis of material with lower crystallite sizes which is a unique feature of  $Nd^{+3}$  doping.

X-ray density ' $D_X$ ' for undoped and Nd doped ferrite samples were determined using following Equation (3).

$$D_X = \left( 8M_x/Na^3 \right) \quad (3)$$

where 'N' is Avogadro's number ( $6.0225 \times 10^{23}$  atoms/mole) and  $M_x$  is the molecular weight of the sample and 'a' is lattice constant. Samples were pressed into pallets (radius 'R' = 5 mm, thickness 't', measured actually with micrometer for each pallet) in order to obtain mass and volume. The mass density ' $D_m$ ' of the materials was calculated using following Equation (4).

$$D_m = \left( M_g / \pi R^2 t \right) \quad (4)$$

where ' $M_g$ ' is the mass of pallet in grams and  $(\pi R^2 t)$  is the volume of pallets.

Porosity 'P' of rare earth doped manganese zinc ferrite nanoparticles in terms of percent was measured using following Equation (5)

$$P = 100[1 - (D_m/D_X)]\% \quad (5)$$

where ' $D_M$ ' is the mass density in g/cc and ' $D_X$ ' is the ' $D_X$ ' is the X-ray density in g/cc.

Calculated values of mass density, X-ray density and porosity were found to be greatly influenced by the inclusion of  $Nd^{+3}$  in the lattice. A linear increase in Mass density and X-ray density that is proportional to increasing Nd concentration was observed in the samples Fig. 2 (a) and (b). However the porosity of the material showed a reverse trend with increasing  $Nd^{+3}$  concentration as shown in Fig. 2 (c). Similar variations as shown in Fig. 2 have been observed by some [38–41] (see Fig. 3).

### 3.2. Bond length and bond angle estimation

As the metal ions occupy two different sites in spinel structure, three types of magnetic interactions are possible, between the cations, through the intermediate  $O^{2-}$  ions, by super-exchange mechanism, namely, A–A interaction, B–B interaction and A–B interaction. The interaction energies are negative and hence induce anti-parallel spin orientation. The magnitude of interaction energy between interacting cations depends upon distances between the cations to the oxygen and the angle between cations distributed over two sites. An angle of  $180^\circ$  will result in greatest exchange energy. Interaction energy decreases rapidly with increasing distances. Out of these three interactions, A–B interaction is the greatest in magnitude and hence the cation anion bond lengths are fairly smaller. A–A interaction is the weakest interaction as the cation anion distance is large.

The bond lengths between metal ions at tetrahedral site and metal at octahedral site denoted as **b**, **c**, **d**, **e** and **f** (bond length

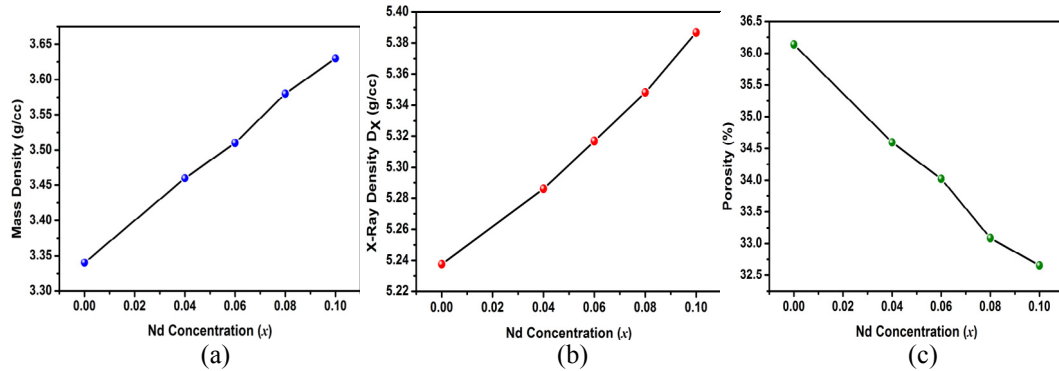


**Fig. 2.** Variation of (a) Mass density (b) X-ray density and (c) Porosity of Mn<sub>0.6</sub>Zn<sub>0.4</sub>Fe<sub>2-x</sub>Nd<sub>x</sub>O<sub>4</sub> with Nd concentration (x).

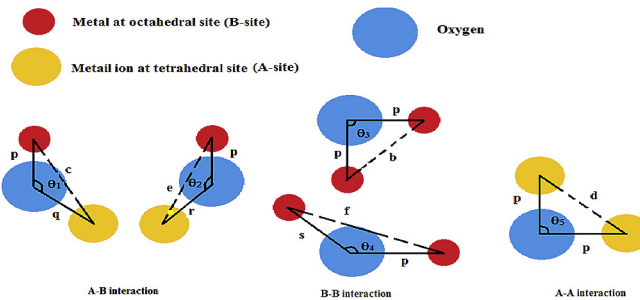


**Fig. 3.** Ion pair configuration in ferrite with bond lengths and angles.

between cations) were estimated in order to investigate the effect of Nd<sup>3+</sup> doping on the structural aspects of the nanoparticles prepared.

These were estimated using Equations (6)–(10) given below where in “a” is a lattice parameter

$$b = \sqrt{2}(a/4) \quad (6)$$

$$c = \sqrt{11}(a/8) \quad (7)$$

$$d = \sqrt{3}(a/4) \quad (8)$$

$$e = \sqrt{3}(3a/8) \quad (9)$$

$$f = \sqrt{6}(a/4) \quad (10)$$

The bond lengths between metal ions and oxygen at various sites are denoted as p, q, r and s (bond lengths between cation-anion) were estimated using following Equations (11)–(14). Here “u” is the oxygen parameter as listed in Table 1.

$$p = a(5/8 - u) \quad (11)$$

$$q = a\sqrt{3}(u - 1/4) \quad (12)$$

$$r = a\sqrt{11}(u - 1/8) \quad (13)$$

$$s = a\sqrt{3}(u/3 + 1/8) \quad (14)$$

The bond angles between cations and cation-anion are denoted as θ<sub>1</sub>, θ<sub>2</sub>, θ<sub>3</sub>, θ<sub>4</sub> and θ<sub>5</sub> and were calculated using following Equations (15)–(19).

**Table 2**  
Variation of bond lengths between cations with Nd<sup>3+</sup> Concentration.

Sample	b (Å)	c (Å)	d (Å)	e (Å)	f (Å)
Mn <sub>0.6</sub> Zn <sub>0.4</sub> Fe <sub>2</sub> O <sub>4</sub>	2.973	3.486	3.641	5.464	5.151
Mn <sub>0.6</sub> Zn <sub>0.4</sub> Fe <sub>1.96</sub> Nd <sub>0.04</sub> O <sub>4</sub>	2.975	3.488	3.643	5.465	5.152
Mn <sub>0.6</sub> Zn <sub>0.4</sub> Fe <sub>1.94</sub> Nd <sub>0.06</sub> O <sub>4</sub>	2.978	3.492	3.648	5.471	5.158
Mn <sub>0.6</sub> Zn <sub>0.4</sub> Fe <sub>1.92</sub> Nd <sub>0.08</sub> O <sub>4</sub>	2.983	3.498	3.653	5.480	5.167
Mn <sub>0.6</sub> Zn <sub>0.4</sub> Fe <sub>1.90</sub> Nd <sub>0.10</sub> O <sub>4</sub>	2.984	3.498	3.654	5.481	5.167

$$\theta_1 = \cos^{-1} \left\{ (p^2 + q^2 - c^2) / 2pq \right\} \quad (15)$$

$$\theta_2 = \cos^{-1} \left\{ (p^2 + r^2 - e^2) / 2pr \right\} \quad (16)$$

$$\theta_3 = \cos^{-1} \left\{ (2p^2 - b^2) / 2p^2 \right\} \quad (17)$$

$$\theta_4 = \cos^{-1} \left\{ (p^2 + s^2 - f^2) / 2ps \right\} \quad (18)$$

$$\theta_5 = \cos^{-1} \left\{ (r^2 + q^2 - d^2) / 2rq \right\} \quad (19)$$

The values of bond lengths and bond angles between cations and cation-anions are listed in Tables 2–4.

Inter atomic distances between the cations at two different sites and cation-anion were found to increase with increasing Nd<sup>3+</sup> concentration as shown in Tables 2 and 3. These variations can be attributed to the larger ionic radii of Nd<sup>3+</sup> ions. The bond angles θ<sub>1</sub>, θ<sub>2</sub> and θ<sub>3</sub> were found to increase indicating the strengthening of A–B and B–B interaction while decreasing values of θ<sub>5</sub> suggest the weakening of A–A interaction [42,43].

### 3.3. Transmission Electron Microscopy (TEM)

Transmission Electron Microscopy (TEM) was employed to determine the size distribution, morphology and crystallinity of the samples. Fig. 4 shows the transmission electron micrographs of

**Table 3**  
Variation of bond lengths between cation-anion with Nd<sup>3+</sup> Concentration.

Sample	p (Å)	q (Å)	r (Å)	s (Å)
Mn <sub>0.6</sub> Zn <sub>0.4</sub> Fe <sub>2</sub> O <sub>4</sub>	2.101	1.820	6.974	3.641
Mn <sub>0.6</sub> Zn <sub>0.4</sub> Fe <sub>1.96</sub> Nd <sub>0.04</sub> O <sub>4</sub>	2.103	1.822	6.976	3.643
Mn <sub>0.6</sub> Zn <sub>0.4</sub> Fe <sub>1.96</sub> Nd <sub>0.06</sub> O <sub>4</sub>	2.108	1.824	6.984	3.648
Mn <sub>0.6</sub> Zn <sub>0.4</sub> Fe <sub>1.92</sub> Nd <sub>0.08</sub> O <sub>4</sub>	2.109	1.826	6.999	3.653
Mn <sub>0.6</sub> Zn <sub>0.4</sub> Fe <sub>1.90</sub> Nd <sub>0.10</sub> O <sub>4</sub>	2.110	1.827	6.999	3.654

**Table 4**

Variation of bond angles between cations and cation-anion with  $\text{Nd}^{+3}$  Concentration.

Sample	$\theta_1$ (degree)	$\theta_2$ (degree)	$\theta_3$ (degree)	$\theta_4$ (degree)	$\theta_5$ (degree)
$\text{Mn}_{0.6}\text{Zn}_{0.4}\text{Fe}_{2}\text{O}_4$	125.251	142.285	92.859	125.276	81.238
$\text{Mn}_{0.6}\text{Zn}_{0.4}\text{Fe}_{1.96}\text{Nd}_{0.04}\text{O}_4$	125.259	142.317	92.861	125.273	81.240
$\text{Mn}_{0.6}\text{Zn}_{0.4}\text{Fe}_{1.96}\text{Nd}_{0.06}\text{O}_4$	125.269	142.322	92.863	125.218	81.241
$\text{Mn}_{0.6}\text{Zn}_{0.4}\text{Fe}_{1.92}\text{Nd}_{0.08}\text{O}_4$	125.243	142.323	92.866	125.185	81.242
$\text{Mn}_{0.6}\text{Zn}_{0.4}\text{Fe}_{1.90}\text{Nd}_{0.10}\text{O}_4$	125.257	142.332	92.869	125.153	81.243

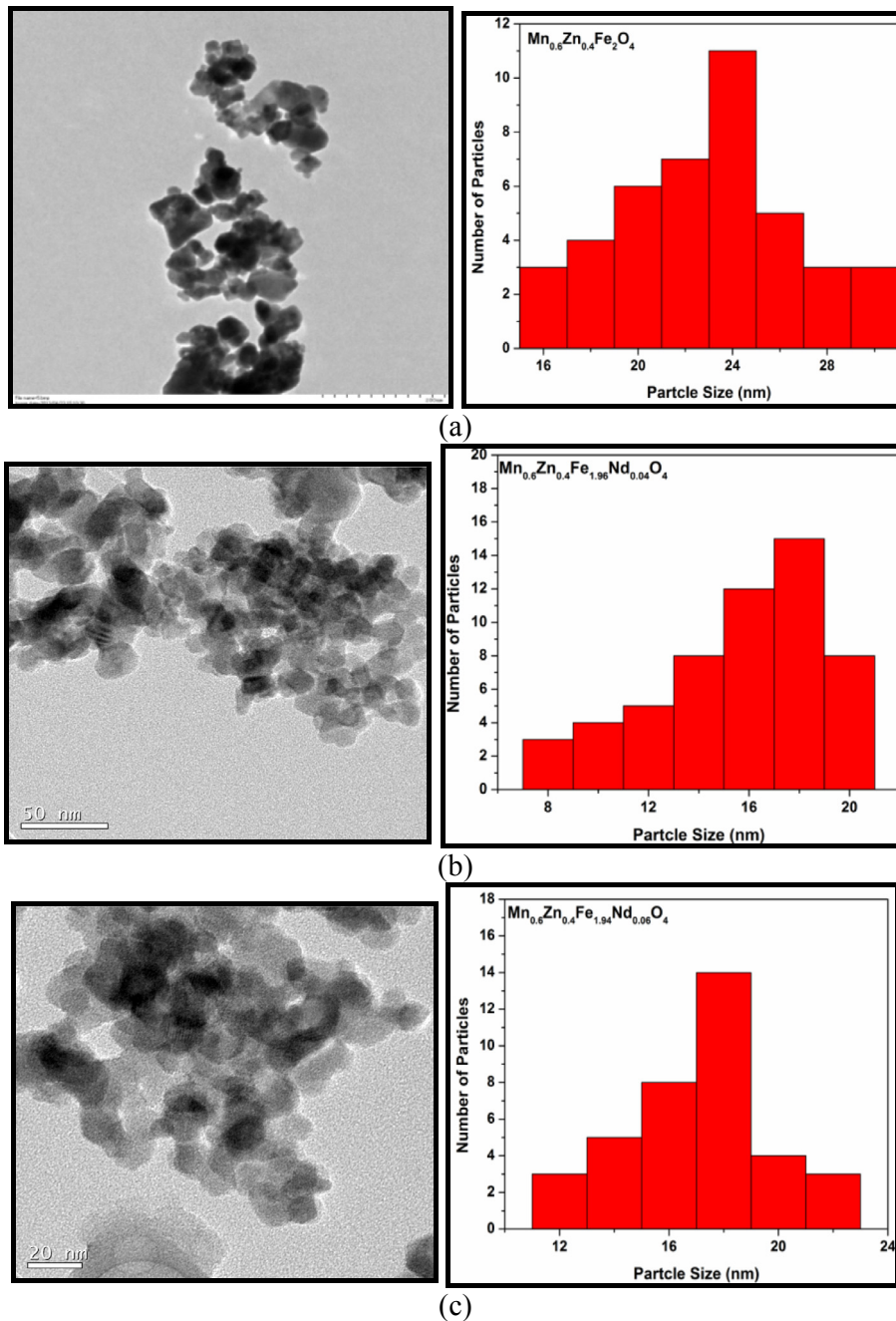


**Fig. 4.** Transmission electron micrographs and particle size distribution of  $\text{Mn}_{0.6}\text{Zn}_{0.4}\text{Fe}_{2-x}\text{Nd}_x\text{O}_4$  with  $x = 0.0, 0.4$  and  $0.6$ .

doped and undoped  $\text{Mn}_{0.6}\text{Zn}_{0.4}\text{Nd}_x\text{Fe}_{2-x}\text{O}_4$ . Rare earth ions that occupy at octahedral site result in strain in the lattice as well as on the grain boundaries causes hindrance in grain growth and results in particle size reduction.

It is can be seen clearly from the Transmission Electron micrographs that due to a strong magnetic character of these samples, large agglomerates of many particles are formed [44,45].

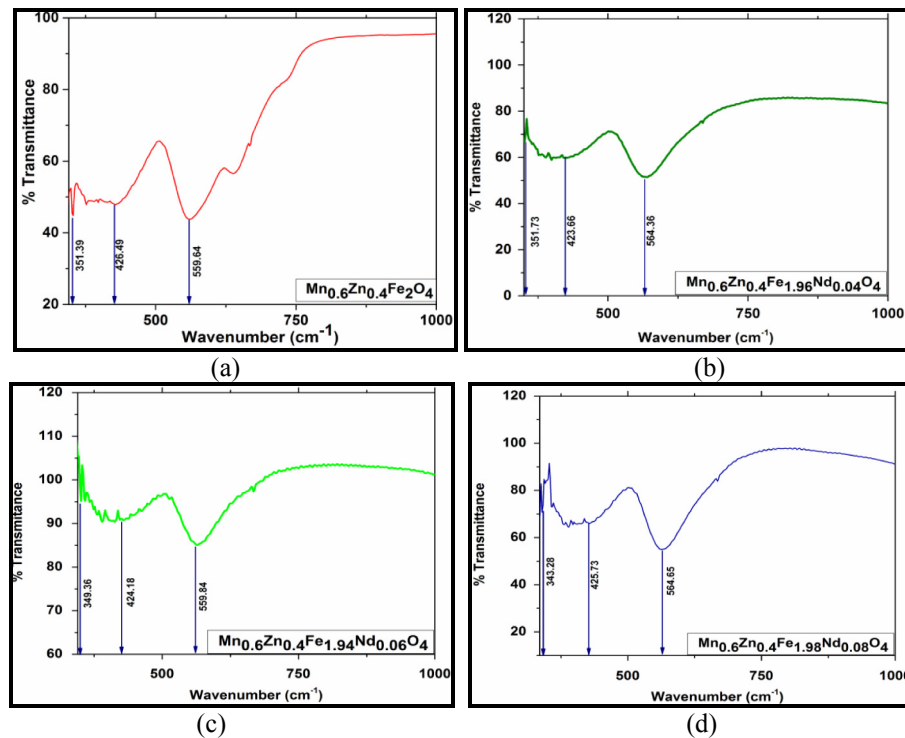


**Fig. 5.** FTIR spectra of  $\text{Mn}_{0.6}\text{Zn}_{0.4}\text{Nd}_x\text{Fe}_{2-x}\text{O}_4$  ferrites.

#### 3.4. Fourier transform infrared spectroscopy

The broad absorption band in the range from  $559 \text{ cm}^{-1}$  to  $565 \text{ cm}^{-1}$  is assigned to  $\text{M}_T-\text{O}$  bond stretching vibration whereas the absorption peak in the range  $424 \text{ cm}^{-1}$  to  $426 \text{ cm}^{-1}$  is due to stretching vibration of metal at  $\text{M}_0-\text{O}$  bond and a band in the range of  $343 \text{ cm}^{-1}$  to  $352 \text{ cm}^{-1}$  is due to  $\text{M}_T-\text{O}-\text{M}_0$  banding vibrations. Where O is oxygen,  $\text{M}_0$  is metal in the octahedral site and  $\text{M}_T$  is metal ion in the tetrahedral site. Presence of three types of vibrational bonds (Fig. 5) in the material that is examined with the absorption band frequencies coinciding with that of spinel ferrite material. It has been observed that substitution of  $\text{Nd}^{3+}$  with  $\text{Fe}^{3+}$  at octahedral site causes shifts of band ( $\text{Fe}^{3+}-\text{O}^{2-}$ ) which is of the type  $\text{M}_T-\text{O}$  bond, towards higher frequency side. This also suggests the occupancy of  $\text{Nd}^{3+}$  at B-sites [46,47].

#### 3.5. Magnetic properties

Magnetic hysteresis loops for  $\text{Mn}_{0.6}\text{Zn}_{0.4}\text{Fe}_{2-x}\text{Nd}_x\text{O}_4$  nanoparticles obtained on vibrating sample magnetometer (VSM) and the variation of saturation magnetization with  $\text{Nd}^{3+}$  concentration are shown in Fig. 6 (a) and (b). The magnetic properties of Mn-Zn ferrite nanoparticles are mainly dominated by the distribution and the magnetic interaction among the cations in the two sub-lattices, namely the tetrahedral (A) and octahedral (B). The inclusion of  $\text{Nd}^{3+}$  ions of large radii into the octahedral lattice sites of the spinel lattice induces cation rearrangement. As per the reports available, the original distribution of the cations in the octahedral and tetrahedral sites may be drastically influenced by the substitution of other ions. Doping of  $\text{Nd}^{3+}$  ions destroys the original cation distribution equilibrium. This rearrangement changes the magnetic moment of octahedral sub lattice and tetrahedral sub lattice favoring the enhancement of magnetic properties of samples due to 3d-4f coupling between Mn, Fe and Nd [48–52].

The magnetic moment per formula unit in Bohr magneton ( $\mu_B$ )

is calculated by using the following relation [53],

$$\eta_B = M_x M_S / (5585) \quad (20)$$

where  $M_x$  is the molecular weight of a particular ferrite composition and  $M_S$  is saturation magnetization (emu/g). In general,  $\text{Nd}^{3+}$  ions have larger ionic radius than  $\text{Fe}^{3+}$ , so the  $\text{Nd}^{3+}$  substitution produces additional strain in the lattice and alters the equilibrium cation distribution at A-site and B-site strengthening A-B causing increase in the  $\eta_B$ .

#### 3.6. Mössbauer spectroscopy

Representative Mössbauer spectra of  $\text{Mn}_{0.6}\text{Zn}_{0.4}\text{Fe}_{2-x}\text{Nd}_x\text{O}_4$  recorded at room temperature in the velocity of  $\pm 11.5 \text{ mm/s}$  using conventional Mössbauer spectrometer are as shown in Fig. 7. Mössbauer spectra for undoped  $\text{Mn}_{0.6}\text{Zn}_{0.4}\text{Fe}_2\text{O}_4$  was fitted into five sextet and a paramagnetic doublet while the spectra for Nd doped samples are fitted with a superparamagnetic doublet and three sextets indicating the alterations in cation distribution due to inclusion of rare earth ion. The presence of these sextets can be attributed to superexchange interaction between the magnetic ions at A- and B-sub-lattices [54].

The presence of Mössbauer active ion in three different environments is confirmed from three sextets along with the paramagnetic doublet in the Mössbauer spectra of rare earth (Nd) doped samples which also confirm the ferrimagnetic nature of the samples.

The broad doublet present in all spectra indicates the existence of super paramagnetic nature in undoped parent sample and all rare earth doped samples. The increase in relative area of super paramagnetic doublet with increasing  $\text{Nd}^{3+}$  concentrations indicates the enhancement in super paramagnetic behavior. Out of remaining three sub-spectra, one corresponds to the tetrahedral site Fe ion and rest two to the octahedral site Fe ion. Out of five

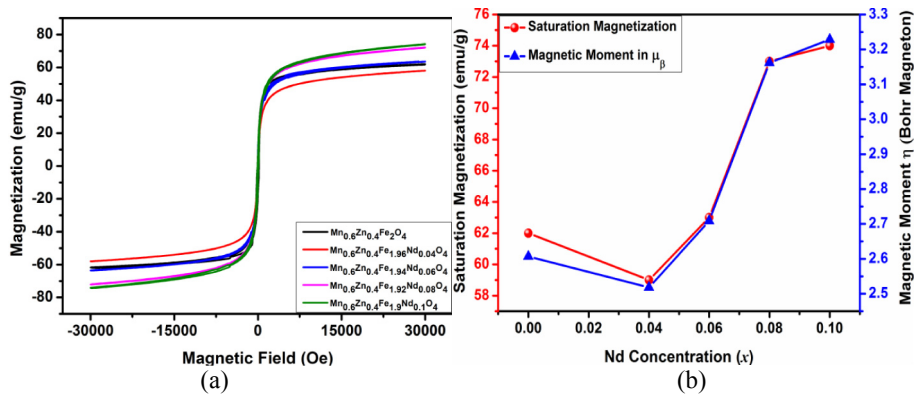


Fig. 6. (a) Hysteresis loops for Mn<sub>0.6</sub>Zn<sub>0.4</sub>Fe<sub>2-x</sub>Nd<sub>x</sub>O<sub>4</sub> obtained on VSM (b) Variation of saturation magnetization.

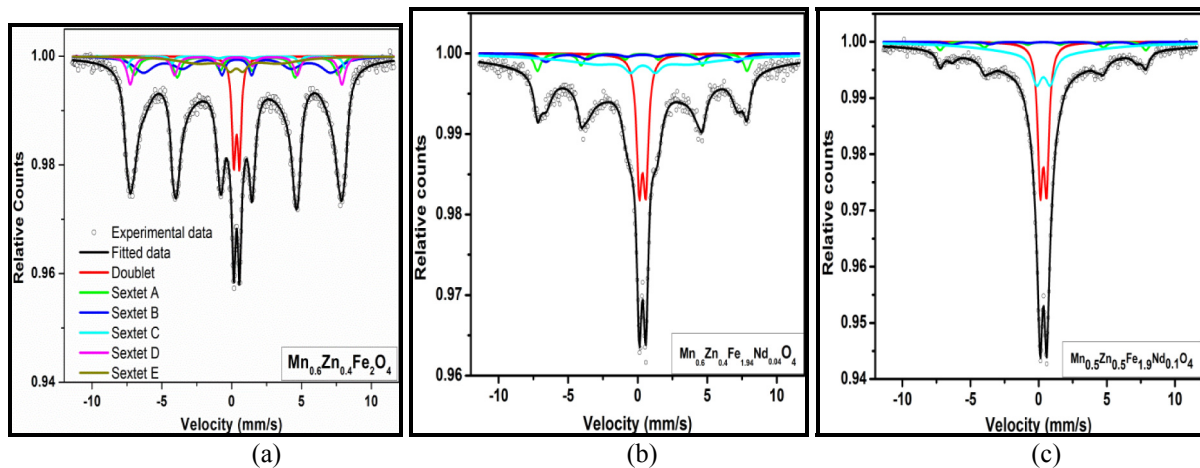


Fig. 7. Mössbauer spectra of Mn<sub>0.6</sub>Zn<sub>0.4</sub>Fe<sub>2-x</sub>Nd<sub>x</sub>O<sub>4</sub> nanoparticles.

**Table 5**  
Calculated values of isomer shift (IS), quadrupole splitting (QS) and hyperfine magnetic field for Mn<sub>0.6</sub>Zn<sub>0.4</sub>Fe<sub>2-x</sub>Nd<sub>x</sub>O<sub>4</sub>.

Sample	Iron site spectra	Isomer shift (IS) mm/s	Quadrupole splitting (QS) mm/s	Hyperfine field (Tesla)	Relative area (%)
Mn <sub>0.6</sub> Zn <sub>0.4</sub> Fe <sub>2</sub> O <sub>4</sub>	Doublet (S. P.)	0.349 ± 0.012	0.072 ± 0.044	—	18.13
	Sextet A (Octa)	0.347 ± 0.017	0.045 ± 0.011	45.06 ± 0.14	16.00
	Sextet B (Octa)	0.313 ± 0.013	0.047 ± 0.015	48.62 ± 0.25	6.44
	Sextet C (Tetra)	0.271 ± 0.021	0.025 ± 0.007	40.09 ± 0.92	23.68
	Sextet D (Octa)	0.341 ± 0.015	0.045 ± 0.013	48.61 ± 0.61	14.95
	Sextet E (Octa)	0.337 ± 0.027	0.046 ± 0.009	47.51 ± 0.45	20.79
Mn <sub>0.6</sub> Zn <sub>0.4</sub> Fe <sub>1.96</sub> Nd <sub>0.04</sub> O <sub>4</sub>	Doublet (S. P.)	0.349 ± 0.002	0.470 ± 0.004	—	35.13
	Sextet A (Octa)	0.398 ± 0.012	0.036 ± 0.008	46.72 ± 0.12	16.84
	Sextet B (Octa)	0.323 ± 0.021	0.046 ± 0.011	42.78 ± 0.31	16.35
	Sextet C (Tetra)	0.293 ± 0.021	0.020 ± 0.003	35.07 ± 0.91	31.68
Mn <sub>0.6</sub> Zn <sub>0.4</sub> Fe <sub>1.94</sub> Nd <sub>0.06</sub> O <sub>4</sub>	Doublet (S. P.)	0.342 ± 0.032	0.448 ± 0.012	—	37.33
	Sextet A (Octa)	0.368 ± 0.042	0.038 ± 0.013	46.98 ± 1.27	16.81
	Sextet B (Octa)	0.333 ± 0.052	0.048 ± 0.006	43.11 ± 1.64	16.66
	Sextet C (Tetra)	0.298 ± 0.029	0.038 ± 0.009	28.33 ± 2.13	29.20
Mn <sub>0.6</sub> Zn <sub>0.4</sub> Fe <sub>1.92</sub> Nd <sub>0.08</sub> O <sub>4</sub>	Doublet (S. P.)	0.348 ± 0.048	0.435 ± 0.018	—	39.61
	Sextet A (Octa)	0.349 ± 0.067	0.043 ± 0.032	47.54 ± 0.88	16.75
	Sextet B (Octa)	0.369 ± 0.066	0.045 ± 0.011	43.66 ± 1.34	16.81
	Sextet C (Tetra)	0.294 ± 0.018	0.047 ± 0.027	20.21 ± 0.98	26.83
Mn <sub>0.6</sub> Zn <sub>0.4</sub> Fe <sub>1.90</sub> Nd <sub>0.10</sub> O <sub>4</sub>	Doublet (S. P.)	0.348 ± 0.048	0.416 ± 0.071	—	41.33
	Sextet A (Octa)	0.337 ± 0.067	0.068 ± 0.017	47.89 ± 0.17	16.69
	Sextet B (Octa)	0.369 ± 0.066	0.047 ± 0.021	43.81 ± 1.23	17.11
	Sextet C (Tetra)	0.289 ± 0.018	0.046 ± 0.033	19.61 ± 1.45	24.87

sextets obtained for undoped parent compound, one sextet corresponds to tetrahedral Fe ion and rest four sextets correspond to Fe ion in octahedral environment. The isomer shift (IS), quadrupole

splitting (QS) and hyperfine field ( $H_{hf}$ ) calculated from the fitting of spectra of Nd doped and undoped samples were calculated.

The isomer shift arises due to the non-zero volume of the

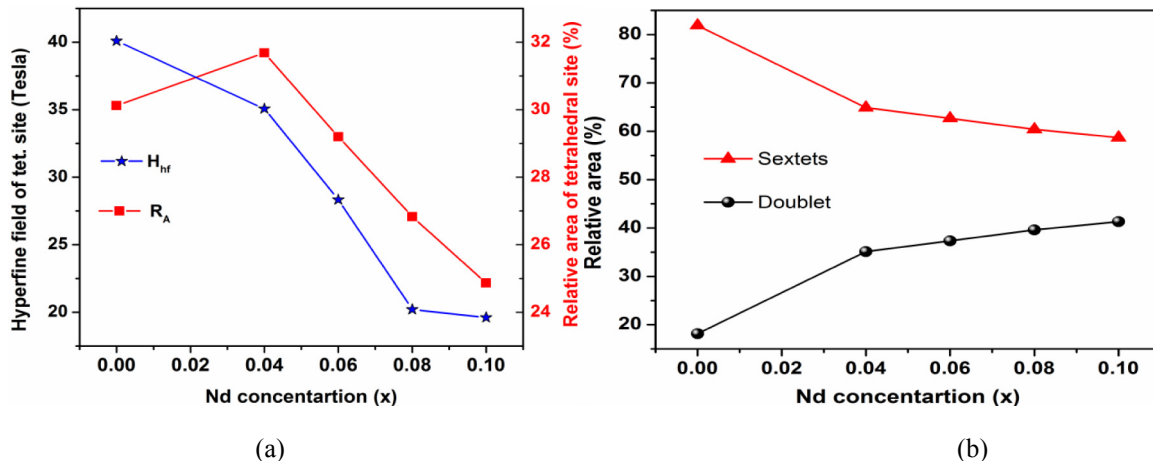


Fig. 8. (a) Variation in area of sextets and doublets with Nd concentration (x). (b) Variation in hyperfine field and relative area of tetrahedral site with Nd concentration (x).

nucleus and the electron charge density due to s-electrons within the vicinity of the nucleus. This leads to a monopole interaction, altering the nuclear energy levels. Any difference in the s-electron environment between the source and absorber thus produces a shift in the resonance energy of the transition. This shifts the whole spectrum positively or negatively depending upon the s-electron density, and sets the centroid of the spectrum. Isomer shift for octahedral (B) sites is more than that of the tetrahedral (A) sites due to larger bond length between  $\text{Fe}^{3+}$ -O in cubic spinel ferrites as compared to that for tetrahedral sites [55]. As a result over lapping of orbitals of  $\text{Fe}^{3+}$  ions is smaller at octahedral (B) sites and thus, a larger IS is produced indicating a higher s-electron density at B site [56]. The isomer shift is a physical parameter for determining the valence state of Mössbauer active atom. It is reported that the isomer shift values for  $\text{Fe}^{3+}$  lie in the range 0.1–0.5 mm/s [57]. By comparing the values in Table 5 for both undoped and Nd doped samples with reported values we can conclude the iron in  $\text{Fe}^{3+}$  state at octahedral and tetrahedral site.

Non-zero quadrupole splitting occur due to chemical disorder in the material which results in an electric field gradient (EFG) of varying magnitude, directions, sign and symmetry. In present study it is observed that paramagnetic doublet appears in all spectra within the sextet due to the interaction of electric field gradient (EFG) with the quadrupole moment of  $^{57}\text{Fe}$  nucleus and reduction in magnetic interaction between iron ions due to inclusion of  $\text{Nd}^{+3}$  ions with greater ionic radii and non magnetic  $\text{Zn}^{+2}$  ions [58–60].

Generally in ferrites B-site hyperfine field is greater than that of A-site and the similar trend was observed in undoped and Nd doped samples. The hyperfine field at B site was found to increase due to inclusion of  $\text{Nd}^{+3}$  at octahedral site where as the hyperfine field at A-site was found to decrease due to iron deficiency caused by rare earth ion inclusion and presence on non magnetic  $\text{Zn}^{+2}$  ion.

The effect of Nd doping was more prominent on tetrahedral site. The hyperfine magnetic field and area of tetrahedral site decreases with increasing Nd concentration as shown in Fig. 8 (a) which confirms that Nd occupies octahedral site. For composition  $x = 0.04$ , large amount Fe ions occupy tetrahedral site, and hence the area of tetrahedral site was found to be maximum for this composition. This is also confirmed from VSM results wherein  $x = 0.04$  shows the lowest value of saturation magnetization ( $M_s$ ) [61]. Increase in relative area of paramagnetic doublet at the expense of relative area of magnetic sextets (Fig. 8 (b)) indicate the enhanced superparamagnetic behavior due to rare earth inculcation at octahedral site.

Cation distribution obtained from Mössbauer spectra of

**Table 6**  
Cation distribution obtained from Mössbauer spectroscopy.

(x)	Cations (Tetrahedral site)	Cations (Octahedral site)
0	$\text{Mn}_{0.12}^{2+}\text{Zn}_{0.4}^{2+}\text{Fe}_{0.48}^{3+}$	$\text{Mn}_{0.48}^{3+}\text{Fe}_{1.52}^{3+}$
0.04	$\text{Zn}_{0.37}^{2+}\text{Fe}_{0.63}^{3+}$	$\text{Mn}_{0.6}^{3+}\text{Zn}_{0.03}^{2+}\text{Fe}_{1.33}^{3+}\text{Nd}_{0.04}^{3+}$
0.06	$\text{Mn}_{0.03}^{2+}\text{Zn}_{0.4}^{2+}\text{Fe}_{0.57}^{3+}$	$\text{Mn}_{0.57}^{3+}\text{Fe}_{1.37}^{3+}\text{Nd}_{0.06}^{3+}$
0.08	$\text{Mn}_{0.08}^{2+}\text{Zn}_{0.4}^{2+}\text{Fe}_{0.52}^{3+}$	$\text{Mn}_{0.48}^{3+}\text{Fe}_{1.40}^{3+}\text{Nd}_{0.08}^{3+}$
0.1	$\text{Mn}_{0.13}^{2+}\text{Zn}_{0.4}^{2+}\text{Fe}_{0.47}^{3+}$	$\text{Mn}_{0.47}^{3+}\text{Fe}_{1.43}^{3+}\text{Nd}_{0.1}^{3+}$

undoped and rare earth (Nd) doped samples is listed in Table 6. It can be seen that the  $\text{Nd}^{+3}$  ions which larger ionic radii have been accommodated at octahedral site by redistributing Mn and Fe ions at tetrahedral site and octahedral site. The reduction of hyperfine field at tetrahedral site can be attributed to the presence on non magnetic  $\text{Zn}^{+2}$  ions along with transfer of Mn on octahedral site weakening A-A interaction.

#### 4. Conclusion

Nanocrystalline powders of rare earth doped manganese zinc ferrite with compositional formula  $\text{Mn}_{0.6}\text{Zn}_{0.4}\text{Fe}_{2-x}\text{Nd}_x\text{O}_4$  were prepared using combustion synthesis. These samples were characterized using XRD, FTIR, TEM, VSM and Mössbauer spectroscopy. Structural parameters like lattice constant, Mass density, X-ray density and crystallite strain were found to increase with increase in  $\text{Nd}^{+3}$  concentrations which can be attributed the larger ionic radii of rare earth ion ( $\text{Nd}^{+3}$ ). Reduction in crystallite size, grain size and material porosity was observed due to introduction of lattice strain and its enhancement as a result of inclusion of rare earth ion in the samples that hindered the grain growth and grain boundaries. Enhancement in saturation magnetization ( $M_s$ ) and magnetic moment per unit formula ( $\eta_B$ ) can be attributed to the cation alteration caused by magnetic rare earth ion ( $\text{Nd}^{+3}$ ) at octahedral site resulting in strengthening of A-B interaction. Low values of Isomer shift and non-zero quadrupole splitting for both undoped as well as rare earth ion ( $\text{Nd}^{+3}$ ) doped samples was evident for the preferred existence of Fe in +3 oxidation state. Inclusion of rare earth magnetic ion with larger ionic radii at octahedral site changes Fe occupancy at octahedral site and tetrahedral site and consequently the Mn concentration on both sites. The manganese and iron deficiency occurring at A site and presence of non magnetic  $\text{Zn}^{+2}$  ions results in reduction in hyperfine field at A-site in the case of rare earth doped samples.

## References

- [1] D.W. Hopkins, A reaction between solids; the formation of zinc ferrite from zinc oxide and ferric oxide, *J. Electrochem. Soc.* 96 (3) (1949) 195–203.
- [2] Xuning Li, Zhaohui Wang, Bo Zhang, Alexandre I. Rykov, Mamdouh A. Ahmed, Junhu Wang,  $\text{Fe}_x\text{Co}_3-x\text{O}_4$  nanocages derived from nanoscale metal–organic frameworks for removal of bisphenol A by activation of peroxyomonosulfate, *Appl. Catal. B Environ.* 181 (February 2016) 788–799.
- [3] R. Arulmurugan, G. Vaidyanathan, S. Sendhilnathan, B. Jeyadevan, Mn–Zn ferrite nanoparticles for ferrofluid preparation: study on thermal–magnetic properties, *J. Magn. Magn. Mater.* 298 (2006) 83–94.
- [4] A. Antic, N. Kremenovic, M.B. Jovic, C. Pavlovic, A.S. Jovalekic, G.F. Nikolic, C. Goya, Weidenthaler, Magnetization enhancement and cation valences in nonstoichiometric  $(\text{Mn},\text{Fe})_{3-\delta}\text{O}_4$  nanoparticles, *J. Appl. Phys.* 111 (2012) 074309.
- [5] Z. Cvejic, S. Rakic, A. Kremenovic, B. Antic, C. Jovalekic, Ph. Colombari, Nanosize ferrites obtained by ball milling: crystal structure, cation distribution, size-strain analysis and Raman investigations, *Solid State Sci.* 8 (2006) 908–915.
- [6] B. Antic, M. Perovic, A. Kremenovic, J. Blanusa, V. Spasovic, P. Vulic, L. Bessais, E.S. Bozin, An integrated study of thermal treatment effects on microstructure and magnetic properties of Zn-ferrite nanoparticles, *J. Phys. Condens. Matter* 25 (8) (2013) 086001.
- [7] M. Vucinic-Vasic, E.S. Bozin, L. Bessais, G. Stojanovic, U. Kozmidis-Luburic, M. Abeykoon, B. Jancar, A. Meden, A. Kremenovic, B. Antic, Thermal evolution of cation distribution/crystallite size and their correlation with magnetic state of Yb substituted Zn-ferrite nanoparticles, *J. Phys. Chem. C* 117 (23) (2013) 12358–12365.
- [8] Ibrahim Sharifi, H. Shokrollahi, S. Amiri, Ferrite-based magnetic nano fluids used in hyperthermia applications, *J. Magn. Magn. Mater.* 324 (2012) 903–915.
- [9] M. Mahmoudi, S. Sant, B. Wang, S. Laurent, T. Sen, Superparamagnetic iron oxide nanoparticles (SPIONs): development, surface modification and applications in chemotherapy, *Adv. Drug Deliv. Rev.* 63 (2010) 24–46.
- [10] H. Mohseni, H. Shokrollahi, Ibrahim Sharifi, Kh. Gheisari, Magnetic and structural studies of the Mn-doped Mg–Zn ferrite nanoparticles synthesized by the glycine nitrate process, *J. Magn. Magn. Mater.* 324 (2012) 3741–3747.
- [11] R.H. Kodama, Magnetic nanoparticles, *J. Magn. Magn. Mater.* 200 (1999) 359–372.
- [12] C.F. Zhang, X.C. Zhong, H.Y. Yu, Z.W. Liu, D.C. Zeng, Effects of cobalt doping on the microstructure and magnetic properties of Mn–Zn ferrites prepared by the co-precipitation method, *Phys. B Condens. Matter* 404 (2009) 2327–2331.
- [13] A.S. Teja, P.-Y. Koh, Synthesis, properties, and applications of magnetic iron oxide nanoparticles, *Prog. Cryst. Growth Charact. Mater.* 55 (2009) 22–45.
- [14] L. Nalbandian, A. Delimitis, V.T. Zaspalis, E.A. Deliyanni, D.N. Bakoyannakis, E.N. Peleka, Hydrothermally prepared nanocrystalline Mn–Zn ferrites: synthesis and characterization, *Microporous Mesoporous Mater.* 114 (2008) 465–473.
- [15] P.P. Hankare, R.P. Patil, U.B. Sankpal, S.D. Jadhav, K.M. Garadkar, S.N. Achary, Synthesis and morphological study of chromium substituted Zn–Mn ferrites nanostructures via sol–gel method, *J. Alloys Compd.* 509 (2011) 276–280.
- [16] D.S. Mathew, R.-S. Juan, An overview of the structure and magnetism of spinel ferrite nanoparticles and their synthesis in microemulsions, *Chem. Eng. J.* 129 (2007) 51–65.
- [17] A. Kale, S. Gubbala, R. Misra, Magnetic behavior of nanocrystalline nickel ferrite synthesized by the reverse micelle technique, *J. Magn. Magn. Mater.* 277 (2004) 350–358.
- [18] P.P. Naik, R.B. Tangsali, B. Sonaye, S. Sugur, Enrichment of magnetic alignment stimulated by  $\gamma$ -radiation in core-shell type nanoparticle Mn-Zn ferrite, *AIP Conf. Proc.* 1512 (2013) 354.
- [19] P.P. Naik, R.B. Tangsali, B. Sonaye, S. Sugur, Radiation stimulated permanent alterations in structural and electrical properties of core-shell Mn-Zn ferrite nanoparticles, *J. Nano Res.* 24 (2013) 194–202.
- [20] Pranav P. Naik, R.B. Tangsali, B. Sonaye, S. Sugur, Sustained augmentation in electrical properties of  $\text{Mn}_x\text{Zn}_{1-x}\text{Fe}_2\text{O}_4$  nanoparticles provoked by high energy gamma radiation, *J. Nano. Adv. Mater.* 3 (No. 1) (2015) 1–7.
- [21] Harinarayan Das, Naonori Sakamoto, Hiromichi Aono, Kazuo Shinozaki, Hisao Suzuki, Naoki Wakiya, Investigations of superparamagnetism in magnesium ferrite nano-sphere synthesized by ultrasonic spray pyrolysis technique for hyperthermia application, *J. Magn. Magn. Mater.* 392 (2015) 91–100.
- [22] O.M. Hemeda, Electrical properties of the Co–Zn ferrites irradiated with  $\gamma$ -rays, *Phase Transit.* 51 (1994) 87.
- [23] O.M. Hemeda, M. El-Saadawy, Effect of gamma irradiation on the structural properties and diffusion coefficient in Co–Zn ferrite, *J. Magn. Magn. Mater.* 256 (2003) 63–68.
- [24] I.M. Hamada, X-ray diffraction and IR absorption in the system  $\text{Co}_{0.6}\text{Zn}_{0.4}\text{Mn}_x\text{Fe}_{2-x}\text{O}_4$  before and after  $\gamma$ -irradiation, *J. Magn. Magn. Mater.* 271 (2004) 318–325.
- [25] H.E. Hassan, T. Sharshar, M.M. Hessien, O.M. Hemeda, Effect of  $\gamma$ -rays irradiation on Mn–Ni ferrites structure, magnetic properties and positron annihilation studies, *Nucl. Instrum. Methods Phys. Res. B* 304 (2013) 72–79.
- [26] L. Ben Tahar, L.S. Smiri, M. Artus, A.-L. Joudrier, F. Herbst, M.J. Vaulay, S. Ammar, F. Fievet, Characterization and magnetic properties of Sm- and Gd-substituted CoFe2O4 nanoparticles prepared by forced hydrolysis in polyol, Mater. Res. Bull. 42 (2007) 1888–1896.
- [27] N. Rezlescu, E. Rezlescu, The influence of Fe substitutions by R ions in a Ni Zn ferrite, *Solid State Commun.* 88 (2) (1993) 139.
- [28] G.L. Sun, J.B. Li, J.J. Sun, X.-Z. Yang, The influences of  $\text{Zn}^{2+}$  and some rare-earth ions on the magnetic properties of nickel–zinc ferrites, *J. Magn. Magn. Mater.* 281 (2004) 173.
- [29] Xu Feng, Zhou Xiangchun, Li Liangchao, Liu Hui, Jiang Jing, Synthesis, magnetic properties and microstructure of Ni-Zn- Cr ferrites doped with lanthanum, *J. Rare Earths* 25 (Jun. 2007) 232.
- [30] R.B. Tangsali, S.H. Keluskar, G.K. Naik, J.S. Budkuley, Effect of sintering conditions on magnetic properties of nanoparticle Mn–Zn ferrite synthesized with nitrilotriacetate precursor method, *Int. J. Nanosci.* 3 (4–5) (2004) 589–597.
- [31] S.H. Keluskar, R.B. Tangsali, G.K. Naik, J.S. Budkuley, High permeability of low loss Mn–Zn ferrite obtained by sintering nanoparticle Mn–Zn ferrite, *J. Magn. Magn. Mater.* 305 (2006) 296–303.
- [32] U.B. Gawas, S.C. Mojumdar, V.M.S. Verenkar, Synthesis, characterization, infrared studies, and thermal analysis of  $\text{Mn}_{0.6}\text{Zn}_{0.4}\text{Fe}_2(\text{C}_4\text{H}_2\text{O}_4)_3 \cdot 6\text{N}_2\text{H}_4$  and its decomposition product  $\text{Mn}_{0.6}\text{Zn}_{0.4}\text{Fe}_2\text{O}_4$ , *J. Therm. Anal. Calorim.* 100 (2010) 867–871 (2010).
- [33] B. Antic, A. Kremenovic, A.S. Nikolic, M. Stoiljkovic, Cation distribution and size-strain microstructure analysis in ultrafine Zn-Mn ferrites obtained from acetylacetone complexes, *J. Phys. Chem. B* 108 (2004) 12646–12651.
- [34] A. Kremenovic, B. Antic, V. Spasovic, M. Vucinic-Vasic, Z. Jaglicic, J. Pirnat, Z. Trontelj, X-ray powder diffraction line broadening analysis and magnetism of interacting ferrite nanoparticles obtained from acetylacetone complexes, *J. Phys. Condens. Matter* 17 (2005) 4285–4299.
- [35] Z. Cvejic, B. Antic, A. Kremenovic, S. Rakic, G.F. Goya, H.R. Rechenberg, C. Jovalekic, V. Spasovic, Influence of heavy rare earth ions substitution on microstructure and magnetism of nanocrystalline magnetite, *J. Alloys Compd.* 472 (2009) 571–575.
- [36] P.P. Naik, R.B. Tangsali, B. Sonaye, S. Sugur, Radiation induced structural and magnetic transformations in nanoparticle  $\text{Mn}_x\text{Zn}_{(1-x)}\text{Fe}_2\text{O}_4$  ferrites, *J. Magn. Magn. Mater.* 385 (2015) 377–385.
- [37] V.D. Mote, Y. Purshotam, B.N. Dole, Williamson-Hall analysis in estimation of lattice strain in nanometer-sized ZnO particles, *J. Theor. Appl. Phys.* 6–6 (2012) 2251–7235.
- [38] C. Venkatraju, Effect of nickel on the structural properties of Mn Zn ferrite nano particles, *Appl. Phys. Res.* 1 (No. 1) (2009) 41–45.
- [39] M.M. Haque, M. Huq, M.A. Hakim, Effect of Cu for Mn on the magnetic properties of Mn-Zn ferrites, *Indian J. Phys.* 78A (3) (2004) 397–400.
- [40] Emad M.M. Ewais, Mahmoud M. Hessien, Abdel-Hady A. El-Geassy, In-situ synthesis of magnetic Mn-Zn ferrite ceramic object by solid state reaction, *J. Aust. Ceram. Soc.* 44 (1) (2008) 57–62.
- [41] K. Rama Krishna, K. Vijaya Kumar, Dachepalli Ravinder, Structural and electrical conductivity studies in nickel-zinc ferrite, *Adv. Mater. Phys. Chem.* 2 (2012) 185–191.
- [42] Z. Karimi, Y. Mohammadifar, H. Shokrollahi, Sh. Khameneh Asl, Gh. Yousefi, L. Karimi, Magnetic and structural properties of nano sized Dy-doped cobalt ferrite synthesized by co-precipitation, *J. Magn. Magn. Mater.* 361 (2014) 150.
- [43] Zein K. Heiba, Mohamed Bakr Mohamed, L. Arda, N. Dogan, Cation distribution correlated with magnetic properties of nanocrystalline gadolinium substituted nickel ferrite, *J. Magn. Magn. Mater.* 391 (2015) 195–202.
- [44] S.R. Naik, A.V. Salker, Change in the magnetostructural properties of rare earth doped cobalt ferrites relative to the magnetic anisotropy, *J. Mater. Chem.* 22 (2012) 2740.
- [45] L. Zhao, H. Yang, X. Zhao, L. Yu, Y. Cui, S. Feng, Magnetic properties of CoFe2O4 ferrite doped with rare earth ion, *Mater. Lett.* 60 (2006) 1–6.
- [46] S.M. Patange, S.E. Shirasath, G.S. Jangam, K.S. Lohar, S.S. Jadhav, K.M. Jadhav, Rietveld structure refinement, cation distribution and magnetic properties of  $\text{Al}^{3+}$  substituted NiFe2O4 nanoparticles, *J. Appl. Phys.* 109 (2011) 053909.
- [47] L. Ben Tahar, L.S. Smiri, M. Artus, A.-L. Joudrier, F. Herbst, M.J. Vaulay, S. Ammar, F. Fievet, Characterization and magnetic properties of Sm- and Gd-substituted CoFe2O4 nanoparticles prepared by forced hydrolysis in polyol, Mater. Res. Bull. 42 (2007) 1888–1896.
- [48] Y.G. Zhang, *Magnetic Materials*, 1988. Chengdu, Pekin (Chapter 1).
- [49] F.X. Cheng, J.T. Jia, Z.G. Xu, B. Zhou, C.S. Liao, L.Y. Chen, H.B. Zhao, Microstructure, magnetic, and magneto-optical properties of chemical synthesized Co-RE (RE=Ho, Er, Tm, Yb, Lu) ferrite nanocrystalline films, *J. Appl. Phys.* 86 (1999) 2727–2732.
- [50] Fuxiang Cheng, Chunsheng Liao, Junfeng Kuang, Zhigang Xu, Chunhua Yan, Liangyao Chen, Haibin Zhao, Zhu Liu, Nanostructure magneto-optical thin films of rare earth (RE = Gd,Tb,Dy) doped cobalt spinel by sol–gel synthesis, *J. Appl. Phys.* 85 (1999) 2782.
- [51] A. Baykal, A.Z. Elmali, M. Sertkol, H. Sözeri, Structural and magnetic properties of  $\text{NiCr}_x\text{Fe}_2-x\text{O}_4$  nanoparticles synthesized via microwave method, *Jer. Superconder. Nover. Magner.* 28 (2015) 3405–3410.
- [52] A. Baykal, F. Genç, A.Z. Elmali, S. Gökçe, M. Sertkol, H. Sözeri,  $\text{MnCr}_x\text{Fe}_2-x\text{O}_4$  nanoparticles: magnetic and microwave absorption properties, *Jer. Inorger. Organomet. Polymer.* 26 (2016) 134–141.
- [53] A.A. Kadam, S.S. Shinde, S.P. Patil, K.Y. Rajpure, Structural, morphological, electrical and magnetic properties of Dy doped Ni–Co substitutional spinel ferrite, *J. Magn. Magn. Mater.* 329 (2013) 59–64.
- [54] D.C. Dobson, J.W. Linnet, M.M. Rahman, Mössbauer studies of the charge transfer process in the system  $\text{Zn}_x\text{Fe}_{3-x}\text{O}_4$ , *J. Phys. Chem. Solids* 31 (12) (1970)

- 2727–2733.
- [55] S.S. Shinde, Sher Singh Meena, S.M. Yusuf, K.Y. Rajpure, Mössbauer, raman, and magnetoresistance study of aluminum-based iron oxide thin films, *J. Phys. Chem. C* 115 (2011) 3731–3736.
- [56] K. Vasundhara, S.N. Achary, S.K. Deshpande, P.D. Babu, S.S. Meena, A.K. Tyagi, Size dependent magnetic and dielectric properties of nano CoFe<sub>2</sub>O<sub>4</sub> prepared by a salt assisted gel-combustion method, *J. Appl. Phys.* 113 (2013) 194101.
- [57] P.P. Naik, R.B. Tangsali, S.S. Meena, Pramod Bhatt, B. Sonaye, S. Sugur, Gamma radiation roused lattice contraction effects investigated by Mössbauer spectroscopy in nanoparticle Mn–Zn ferrite, *Radiat. Phys. Chem.* 102 (2014) 147–152.
- [58] S.R. Naik, A.V. Salker, S.M. Yusuf, S.S. Meena, Influence of Co<sup>2+</sup> distribution and spin–orbit coupling on the resultant magnetic properties of spinel cobalt ferrite nanocrystals, *J. Alloys Compder.* 566 (2013) 54–61.
- [59] Shalendra Kumar, A.M.M. Fare, Khalid Mudasam Batoo, Chan Gyu Lee, B.H. Koo, Ali Yousef, Alimuddin, Mössbauer studies of Co<sub>0.5</sub>CdxFe<sub>2.5-x</sub>O<sub>4</sub> (0.0 ≤ x ≤ 0.5) ferrite, *Phys. B* 403 (2008) 3604–3607.
- [60] D.E. Dickson, F.J. Berry, Mössbauer Spectroscopy, Cambridge University Press, London, 1986, p. 22.
- [61] M.M. Eltabey, W.R. Agami, H.T. Mohsen, Improvement of the magnetic properties for Mn–Ni–Zn ferrites by rare earth Nd<sup>3+</sup> ion substitution, *J. Adv. Res.* 5 (2014) 601–605.